

Full-scale experimental study on precast bridge column with grouted sleeve connections and large-diameter reinforcing bars

Penghui Zhang^a, Zhiqiang Wang^a, Jiping Ge^{b,*}, Xingfei Yan^c, Side Liu^d

^a Dept. of Bridge Engineering, Tongji Univ., 1239 Siping Rd., Shanghai 200092, China

^b School of Urban Construction and Safety Engineering, Shanghai Institute of Technology, 100 Haiquan Rd., Shanghai 201418, China

^c Shanghai Urban Construction Design Research Institute (Group) Co., Ltd., 3447 Dongfang Rd., Shanghai 200125, China

^d China Railway 22nd Bureau Group 3rd Engineering Co., Ltd., 166 Tapu East Rd., Xiamen 361000, China

ARTICLE INFO

Keywords:

Full-scale experiment
Precast bridge column
Grouted splice sleeve connection
Strain penetration effects
Ultimate bearing capacity

ABSTRACT

In this study, a full-scale bridge column with grouted sleeve (GS) connections and large-diameter (40 mm) reinforcing bars was investigated experimentally and numerically with comparison to a reference cast-in-place (CIP) column. Finite element models were established at the *OpenSeesPy* platform and validated against experimental results. Consequently, empirical equations are developed to predict effective rotational stiffness, post-yield stiffness ratio, ultimate moment, and ultimate rotation of joint sections. And the predicted parameters by empirical equations are compared with the calibrated parameters from the numerical analysis results. Finally, a simplified bilinear rotational spring was proposed to simulate strain penetration in GS and CIP columns. The availability of the simplified simulation method of strain penetration effects was confirmed with the numerical simulation results of full-scale tests. Results indicate that the failure mode, crack pattern, deformation, and resistance mechanism of the GS column are different from that of the CIP column. The first yield and maximum lateral load of the GS column are 6%, 5% larger than the CIP column, and the ultimate lateral displacement of the GS column is 96% of the CIP column. The numerical models generally matched well with the load-displacement curves and joint opening of tested columns. The simplified bilinear rotational spring with predicted parameters is effective in simulating strain penetration in GS and CIP columns.

1. Introduction

In recent years, accelerated bridge construction (ABC), which relies heavily on prefabricated reinforced members, has gained substantial attention for several potential advantages of reduced onsite construction time, less traffic impact, higher construction quality, etc. For ABC piers, the connections between precast members and foundations have a crucial effect on structural integrity and seismic performance since connections are located in the plastic region under seismic load. Various connection types are proposed, including bar coupler connections, grouted corrugated duct connections, prestressed connections, pocket/socket connections, and so on. Among these connections, grouted sleeve (GS) connections with grouted splice sleeve couplers (GSSCs) at the pier bottom are widely applied because of convenient construction and clear force transfer mechanism. A few experimental, numerical, and theoretical studies have been conducted to reveal the seismic performance of GS columns.

Quasi-static cyclic test results indicated that the damage of precast columns with GS connections is concentrated on the ends of GSSCs, leading to lower displacement ductility and energy dissipation capacity than the cast-in-place (CIP) specimen [1–3]. The flexural strength of GS specimens was higher than reference CIP specimens due to the compressive strength contribution of GSSCs [4]. Based on quasi-static and shake table tests, improved ductile performance and different damage mechanisms were observed when GSSCs were located inside the column bottom rather than the footing [5,6]. To enhance the ductility of GS columns, bar debonding at the column-to-footing interface was adopted to reduce strain localization by Ameli et al. [3], and the effectiveness was then validated. Haber et al. [7] proposed a design method that shifts the plastic hinge above the connection region by using high-strength protruding footing bars, and good ductility was acquired. Liu et al. [8] also achieved relocation of the plastic hinge in accordance with adding a grouted central tenon at the pier end. But it is noteworthy that hinge relocation is sensitive to shear-critical columns. Wang et al. [9]

* Corresponding author.

E-mail addresses: penghui@tongji.edu.cn (P. Zhang), wangzhiq@tongji.edu.cn (Z. Wang), bridgejiping@126.com (J. Ge).

have studied the seismic performance of precast bridge columns with various shear span-to-depth ratios of 1.7, 0.85, and 0.6. Short columns with a height lower than the plastic hinge region were found to suffer pure shear failure, while the others exhibited combined bending and shear failure. The aforementioned scaled test results are influenced by the size effect, so Wang et al. [10] conducted a quasi-full scale experimental study on GS bridge piers with a shear span ratio of 3.125 to solve this issue. Full-scale sliced columns were used to substitute prototype columns. The peak load of the GS column was 14% less than the CIP column, which is inconsistent with scaled test results [3,4,6]. Considering mechanical behaviors of reinforced concrete structures are deeply impacted by the size effect, existing results of scaled bridge pier tests need to be validated by full-scale tests.

The numerical studies are focused on simulating the mechanical behaviors of GSSCs and GS columns accurately and efficiently. Several bond-slip models for GSSCs were proposed and verified with experimental data [11–15]. Haber et al. [16] found linear relationships between strain over the coupler region and reinforcing bar strain away from the coupler region. Then, elastic and plastic scaling factors were introduced for modeling GSSCs in reinforced concrete members. Tazav and Saiidi [17] proposed another strain modification method accounting for the coupler effect. It was assumed that a portion of the coupler (βL_{sp} , where L_{sp} is the length of GSSCs) is rigid, and the remaining portion contributes to the axial deformation of the splice. The suggested rigid length factor β is 0.65 for GSSCs. Culmo et al. [18] concluded that GSSCs could be simulated as amplified steel bars whose section areas combined grouted sleeves and longitudinal bars. Based on reliable finite

element models, the mechanical performance of GS columns was further investigated, such as lateral loading capacity, displacement capacity, and ductility. Tazav and Saiidi [17] proposed a modified plastic hinge length formula for GS piers based on the rigid length factor β . Wang et al. [19] indicated that the factor β should be linearly dependent on pier height when pier height is less than 11 m, and a β of 1.394 is suggested for piers higher than 11 m. Besides, Ding et al. [20] proposed a deformation capacity estimation method for rectangular-section columns considering the deformation of two plastic hinges at the ends of GSSCs, respectively. However, the deformation demand estimation for GS piers is still tedious for bridge designers because of the challenge of simulating joint behavior.

In this study, a full-scale specimen including GS and CIP columns was tested to eliminate the influence of the size effect. The backbone curves, crack patterns, and strains of reinforcement and concrete were exhibited and compared sequentially. Finite element models were established at the *OpenSeesPy* platform and validated against experimental results. Finally, a simplified bilinear rotational spring was proposed to simulate strain penetration in GS and CIP columns.

2. Description of the test specimen

2.1. Specimen design

The specimen design is based on the actual segmental expressway bridge in Shaoxing. The specimen consists of a full-scale reference CIP column, a full-scale GS column, and a reaction column. The material,

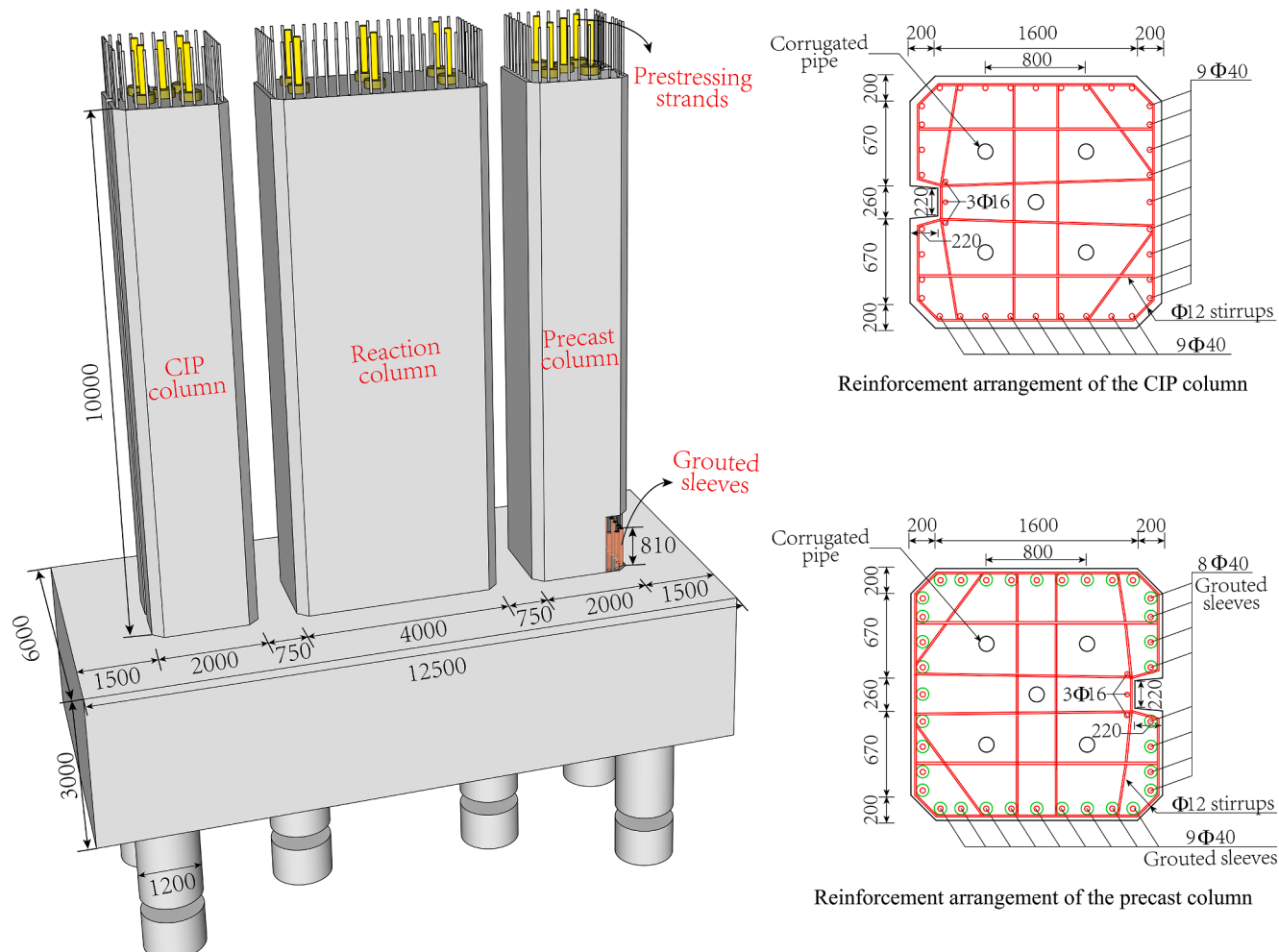


Fig. 1. Dimensional and structural details of the test specimen (all dimensions are in millimeters).

geometry, producing, assembling, and grouting of the GS column are the same as prototype bridge piers. For comparative purposes, the CIP column has identical dimensions to the precast one. As shown in Fig. 1, tested columns have a 2.0×2.0 m rectangular cross-section and a height of 10 m. There is a trapezoidal notch on the pier section for pipeline installation. A 2.0×4.0 m cross-section reaction column is arranged between the precast and CIP columns so that tested columns can experience ultimate strength while the reaction column is undamaged. The specimen is supported by six 1.2-m-diameter drilled grouting piles and a $12.5 \times 6.0 \times 3.0$ m pile cap. The pile length is 40 m.

Tested columns are designed to construct with C40 (characteristic prismatic compressive strength $f_{ck} = 26.8$ MPa) concrete and HRB400 (characteristic yield strength $f_{sk} = 400$ MPa) steel bars. Thirty-five 40-mm-diameter longitudinal steel reinforcements are annularly assembled in the tested column section leading to a longitudinal reinforcement ratio of 1.23%. Three 16-mm-diameter bars are arranged around the trapezoidal notch and truncated at the bottom of the tested columns. 40-mm-diameter longitudinal bars are directly anchored in the pile cap for the CIP column. In the GS column, they are connected to the protruding bars of the pile cap through GSSCs. The GSSC is a hollow cast iron sleeve connecting each component's bars. Axial forces of dowel bars are transferred by bond stress between bars, grout, and sleeve. The details of GSSCs used in the specimen are shown in Fig. 2. A 2 cm bedding mortar layer is inserted between the GS column and pile cap to prevent joint corrosion. The column stirrup is densified from 1.0 m down the column bottom to 2.0 m up the column bottom. The 12-mm-diameter stirrup spacing is 0.1 m and 0.15 m in densified and non-densified regions, corresponding to a transverse reinforcement ratio of 0.85% and 0.57%, respectively. Piles and the pile cap are constructed with C30 (characteristic prismatic compressive strength $f_{ck} = 20.1$ MPa) concrete.

2.2. Construction of the specimen

The construction processes of the specimen are shown in Fig. 3. Most specimen components are cast in place except for the GS column. First, the pile group foundation was constructed at the experimental site while the unbonded PT strands penetrated through the pile cap with an end anchored in the bottom. The reinforcement cages of the CIP and reaction columns were subsequently produced, followed by mold forming, concrete casting, mold removing, and specimen curing. In order to reduce local compressive stress at the loading point, a steel plate was settled on the column surface, as illustrated in Fig. 3(b). The arrangement of unbonded PT strands biases the design due to construction errors, as shown in Fig. 3(c). The fabrication and installation process of the GS column is exhibited in Fig. 3(d)-(i). It was made first by forming the reinforcement cage and casting C40 concrete. After curing for 28 days, the precast segment was assembled by inserting 40-mm-diameter protruding longitudinal bars into the corresponding GSSCs. Finally, high-strength non-shrinkage grouting material was grouted into the sleeves. The grouting plumpness was detected with the embedded sensor method [21]. The detection results indicated an excellent grouting quality. It is noteworthy that a 3 cm stop-grouting plug is set at the end of grouted sleeves, and a 2 cm bedding mortar layer is formed between the pile cap and GS column. Consequently, dowel bars protruding from the pile cap were debonded from surrounding concrete over a 5 cm region just below the GS column.

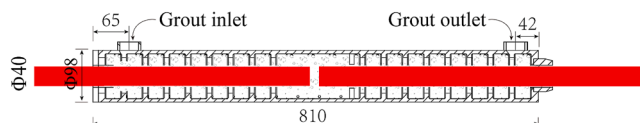


Fig. 2. Details of the GSSC (all dimensions are in millimeters).

2.3. Material properties

According to the Chinese code standard for the test method of mechanical properties of normal concrete [22], three $150 \times 150 \times 150$ mm concrete cubes for each tested column were collected and standard cured. The average test-day compressive strengths of the CIP column and GS column cubes were 46.5 MPa and 64.5 MPa, respectively. The test-day compressive strength of grouting material was 115 MPa tested with a test block dimension of $40 \times 40 \times 160$ mm [23]. The reinforcement properties were acquired based on the Chinese code [24]. The yield strength, ultimate strength, and break elongation of steel bars are given in Table 1.

Before applying GSSCs to the specimen, the performance of GSSCs with various embedded lengths (e.g., $6D_s$, $7D_s$, $8D_s$, $10D_s$, where D_s is the diameter of connected bars of 40 mm) was investigated through experimental studies. Then a proper embedded length was selected to avoid bar pull-out failure and sleeve fracture during the full-scale quasi-static test. The test setup is shown in Fig. 4. Two GSSC specimens were tested for each embedded length. Every specimen was loaded under cyclic loading at high stress [25]. Nominal yield stress, ultimate stress (loading forces divided by section area of embedded bars), and failure pattern are listed in Table 2. A GSSC with an embedded length of $6D_s$ failed due to bar pull-out, while others failed because of bar fracture. An embedded length of $7D_s$ is long enough to prevent bar pull-out failure. However, the practical construction environment is more complex than the ideal one used in the test, resulting in various construction defects and eccentricity, which may affect the tensile load capacity of GSSCs [14,26]. The *Technical Specification for Prefabricated Bridge* [27] suggests the practical embedded length should be $10D_s$. So an embedded length of $10D_s$ was applied to the GS column design.

2.4. Test setup and instrumentation

The CIP column and the GS column were subjected to static unidirectional loading successively at an actual bridge construction site. The test setup is illustrated in Fig. 5. The loading point is located at 9.5 m above the column-to-foundation interface leading to a shear ratio of 4.75. To acquire sufficient load capacity, three jacks were adopted to provide lateral load and were controlled by one oil pump. Jacks were mounted between the tested column and the reaction column. And they were suspended to the support frame fixed to protruding bars on the pier top. The maximum load capacity and stroke of jacks are 2000 kN and 500 mm. Moreover, spherical hinges were set at each end of jacks to accommodate pier top rotation during the test, as shown in Fig. 6. Five 2660-mm²-area unbonded post-tensioned (PT) strands with an ultimate strength of 1860 MPa were used to produce an axial force of 12,875 kN on each tested column, corresponding to a design axial load ratio of 17.6%. The axial load value was determined based on the self-weight of the superstructure and secondary dead load acting on the reference bridge column used in real bridge structures.

A trial load of 150 kN was applied once to check jacks and the data acquisition system before the formal unidirectional loading. Tested columns were tested with a predefined loading protocol inspired by Wang et al. [10]. To study mechanical behavior during the serviceability stage, a forced-controlled monotonic load was first applied with a loading step of 50 ~ 300 kN. Once the lateral load reached 2550 kN, the loading procedure was controlled by displacement of 10 mm, 20 mm, 50 mm, 100 mm, 150 mm, 200 mm, and so forth. The loading was paused at each loading step to mark cracks and measure crack widths. Tests were terminated when the applied load was reduced to 85% maximum lateral load. Discrete loading data were collected by a multifunction data acquisition system, including loads, displacement, curvature, and strains. Two displacement meters and five prisms were installed on the surface of each tested column. The column deformation was measured by displacement meters and an electronic total station. The measurement precision was checked by each other. Joint opening was measured



Fig. 3. Fabrication and installation of the GS column: (a) foundation; (b) reinforcement cage of the CIP column and the reaction column; (c) PT strands of CIP column; (d) reinforcement cage of the GS column; (e) arrangement of longitudinal reinforcement; (f) GS column after removing mold; (g) protruding bars of the pile cap; (h) assembly of the GS column to pile cap; (i) grouting into the sleeves.

Table 1
Properties of reinforcing steel bars.

Specimen	Diameter (mm)	Yield strength (MPa)	Ultimate strength (MPa)	Elongation at break (%)
CIP column	12	435	605	21.0
	40	450	660	17.3
GS column	12	485	665	15.2
	40	460	675	13.8

using displacement meters located at the column end. A crack width detector was used as assistance when it was not significant. As the joint opening exceeded the measuring range of the crack width detector, a steel ruler was employed for verification.

3. Test result and discussion

3.1. Crack patterns and failure modes

The two tested columns exhibited distinct crack patterns and failure modes. In the case of the conventionally CIP column, the first crack

appeared at the interface between the column and foundation when the lateral load reached 705 kN. This crack then propagated along the tensile portion of the column section, reaching a maximum width of 3 mm at the lateral force of 3215 kN. All major flexural cracks have been developed until the loading step of 2550 kN, and vertical cracks appeared on the compression side simultaneously. The cracks continued to develop, widen, and connect, forming a final crack pattern like Fig. 7 (a). Subsequently, the longitudinal bars fractured after reaching the maximum lateral load of 3521 kN (Fig. 8). Once the lateral load capacity decreased to 85% of the maximum value, the test was terminated at a lateral displacement of 720.2 mm. At the end of the test, spalling of the compression-side cover concrete occurred over a height of 1.4 m above the column-to-footing interface.

In contrast, the GS column exhibited few flexure cracks along the height of the GSSC region due to the strengthening of grouted splice sleeve. Damage in the GS column was mainly concentrated at the top and bottom of the GSSCs. The cracks initiated at the bedding mortar between the column and foundation at a lateral load of 675 kN. The first flexure crack of the pier body occurred at the height of 1.1 m from the column base when the lateral load reached 1200 kN. Similar to the CIP column, major flexural cracks have been developed until the end of the 2550 kN later load. Concrete compressive crushing began at a lateral

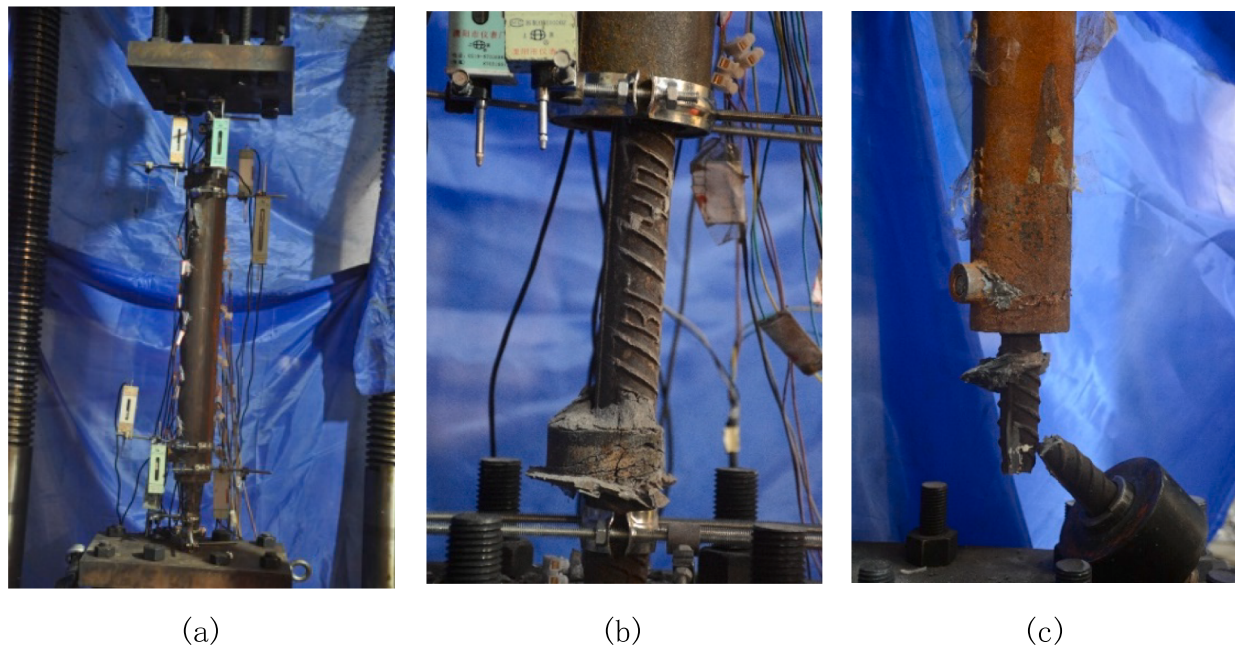


Fig. 4. Test of GSSCs: (a) test setup; (b) bar pull-out; (c) bar fracture.

Table 2
GSSC strength and failure patterns under cyclic loading at high strength.

Specimen	Embedded length (m)	Yield force (kN)	Yield stress (MPa)	Ultimate force (kN)	Ultimate stress (MPa)	Failure pattern
1	$6D_s$	538.3	428.4	783.5	623.5	Bar fracture
2	$6D_s$	555.9	442.4	786.2	625.6	Bar pull-out
3	$7D_s$	534.3	425.2	786.4	625.8	Bar fracture
4	$7D_s$	538.2	428.3	786.0	625.5	Bar fracture
5	$8D_s$	544.2	433.1	789.9	628.6	Bar fracture
6	$8D_s$	542.0	431.3	786.0	625.5	Bar fracture
7	$10D_s$	540.3	430.0	809.6	644.3	Bar fracture
8	$10D_s$	545.3	433.9	809.5	644.2	Bar fracture

displacement of 100 mm, followed by spalling at 200 mm displacement, which propagated along a height of approximately 1.2 m until the end of the test. The joint opening reached 12 mm at the maximum lateral load. Unexpectedly, the 90-degree hooks of stirrups near the top of the GSSC straightened, followed by the buckling of the longitudinal bars at the top of the GSSC, as depicted in Fig. 9. The failure of stirrups resulted in insufficient confinement to longitudinal bars, aggravated the buckling of longitudinal bars. As a result, the lateral load capacity decreased rapidly with no longitudinal bar fracture. The final crack pattern is illustrated in Fig. 7(b). Cracks were observed to be concentrated around the top of the GSSCs, indicating a notable occurrence of localized damage. It is worth realizing that 135-degree hooks were fabricated in the CIP column according to Chinese code [28]. But unwelded 90-degree hooks were used in the GSSC region of the GS column for construction convenience. The stirrups were not densified around the top of GSSC. The longitudinal bars have a diameter of 40 mm, requiring stronger lateral confinement than the longitudinal bars with minor diameters used in previous sub-scale specimens. Experiment results indicate stirrups with 90-degree hooks should be welded into closed stirrups at the region of the GSSC.

In addition, more stirrups are conservatively suggested to arrange around the top of GSSC.

3.2. Lateral load–displacement relationships

The lateral load versus displacement relationships of tested columns are illustrated in Fig. 10. Four critical limit states were detected from the backbone curves: (1) initial cracks appeared; (2) first yield of longitudinal bars; (3) maximum lateral load reached; (4) the applied load was reduced to 85% maximum lateral load, and ultimate lateral displacement was reached. Table 3 summarizes the later loads and displacement of the four limit states. The GS column exhibited a 6% and 5% higher first yield and maximum lateral load, respectively, compared to the CIP column. This can be attributed to the strengthening provided by the GSSCs and the increased material strength. The reduced strain concentration of longitudinal bars at the column-to-foundation intersection, due to a 5 cm debonding length, resulted in delayed bar yield and fracture, leading to greater lateral displacement. However, the ultimate lateral displacement of the GS column is 96% of the CIP column due to differences in failure modes. The CIP column exhibited a typical flexural failure with the longitudinal bar fracture, while the GS column presented a failure by bar buckling and concrete crush induced by stirrup straightening without longitudinal bar fracture. Additionally, the concrete elastic modulus of the GS column is 18% higher than the CIP column, which means lateral displacement induced by column flexure is decreased. As shown in Fig. 11, column deformation within a height of approximately 4.0 m at the column base is predominated by rigid rotation induced by joint opening. The displacement of the pier top is impacted by both column flexure and rigid rotation. As a result, the GS column exhibited larger deformation in the lower part column and smaller displacement at the pier top when tested columns were subject to the same lateral load. Compared to the CIP column, deformation of the GS column was concentrated on the ends of GSSCs, while the local region enhanced by GSSCs showed negligible curvature, as illustrated in Fig. 12.

In addition, the equivalent yield points were calculated by idealizing lateral load–displacement curves based on equal energy dissipation principles, as shown in Fig. 10 [29]. The displacement ductility, defined as the ratio of ultimate displacement to yield displacement, was found to be 5.6 for the GS column and 6.1 for the CIP column. The displacement

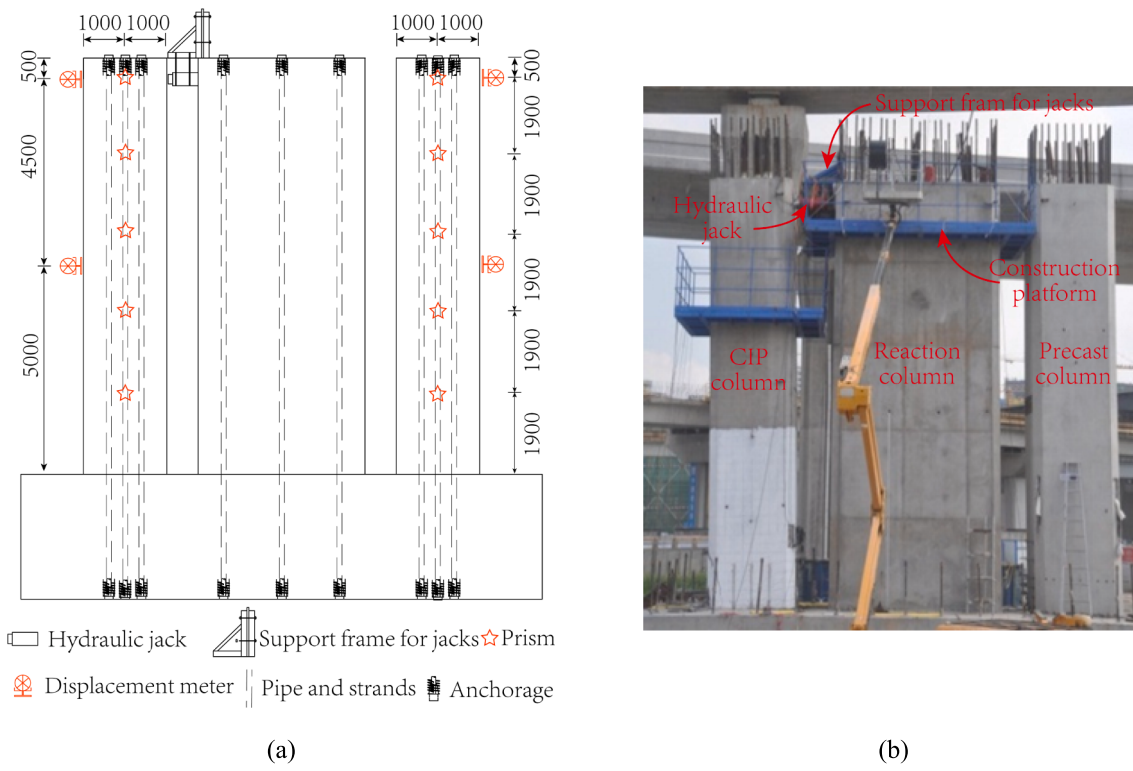


Fig. 5. Test setup (unit: mm): (a) schematic of test setup; (b) actual setup.

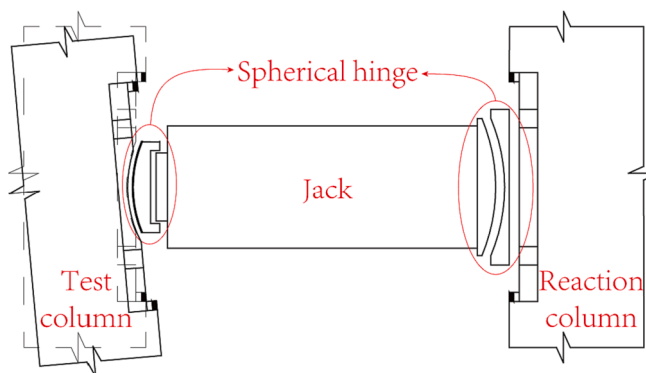


Fig. 6. Arrangements of jacks.

ductility of the GS column exceeded the minimum requirement of 4.0 specified for precast piers in high seismic zones, as stipulated by the Chinese code for the seismic design of urban bridges.

3.3. Strain of reinforcements and concrete

Fig. 13 shows the measured concrete strains in critical sections of tested columns (e.g., column-to-foundation section, GSSC top section with a height of 0.82 m to pier bottom). Cover concrete began to crush once compressive stress reached the compressive strength corresponding to a strain of $2000\mu\epsilon$. So strains exceeded $2000\mu\epsilon$ were not measured. The CIP column presented a more extensive concrete strain at GSSC top section compared to the column-to-foundation section. This phenomenon coincides with the assumption of the lumped plastic hinge model that the rotation center is located in the middle of the plastic hinge. The measured maximum compressive strain of the GS column appeared at the column-to-foundation section due to the rigid rotation at the pier bottom. But concrete spalling occurred first at the top of GSSCs as a result of the insufficient lateral confinement.

Strain distributions of the longitudinal reinforcement are shown in Fig. 14. The reference height of 0.0 m is set at the interface between the column and foundation. Yield strains can be acquired through elastic modulus and yield stress from the material property tests. For the CIP column, the maximum bar strain occurred at the pier bottom, and strain

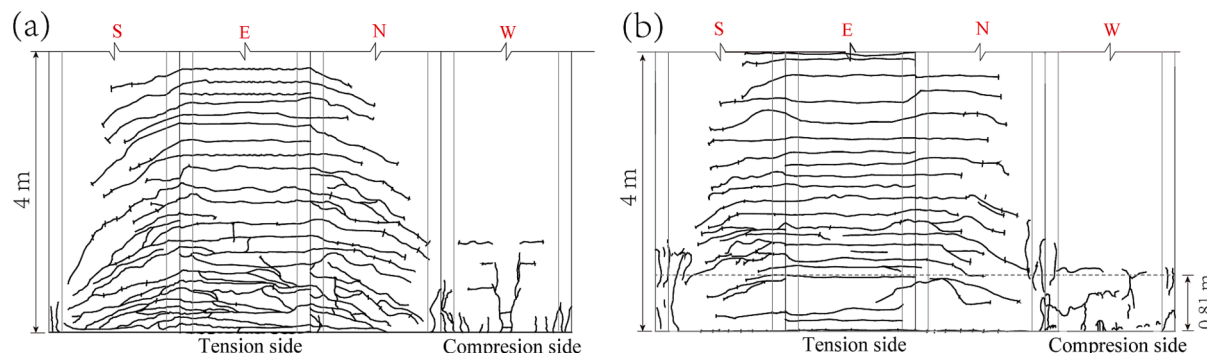


Fig. 7. Crack patterns: (a) CIP column; (b) GS column.



Fig. 8. Post-test damage of the CIP column.



Fig. 9. Post-test damage of the GS column.

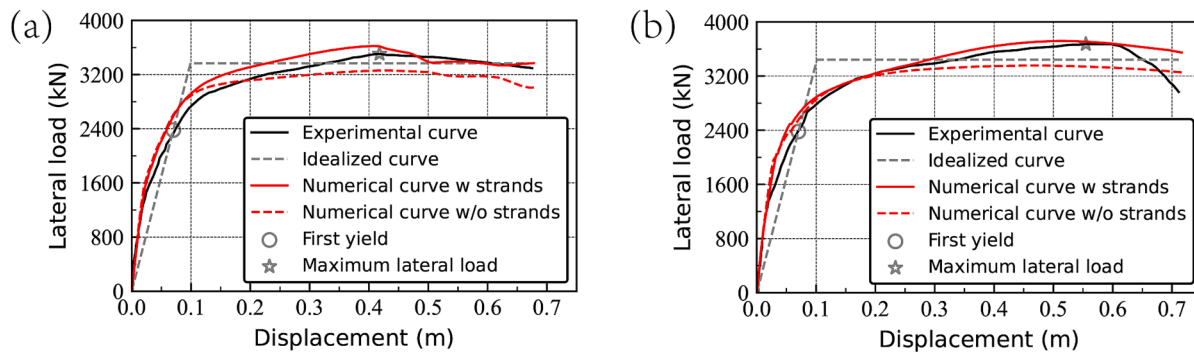


Fig. 10. Lateral load-displacement curves: (a) CIP column; (b) GS column.

Table 3
summary of test results.

Limit state	GS column		CIP column		GS-to-CIP ratio	
	Load (kN)	Disp. (mm)	Load (kN)	Disp. (mm)	Load	Disp.
Initial cracks appeared	675	4.5	705	6.9	0.96	0.65
First yield of longitudinal bars	2520	76.1	2381	70.1	1.06	1.07
Equivalent yield point	3442	101.3	3369	99.2	1.02	1.02
Maximum lateral load reached	3690	571.4	3521	420.9	1.05	1.36
Ultimate lateral displacement reached	3137	696.7	2993	720.2	1.05	0.96

penetrations were observed due to bond-slip behavior. Longitudinal reinforcement simultaneously yielded at both ends of GSSCs in the GS column, indicating a different plastic hinge mechanism from the CIP column.

4. Numerical simulation and evaluation

The FE model of the studied full-scale specimens described previously is generated in the *OpenSeesPy* platform [30], as illustrated in Fig. 15. The column is modeled using displacement-based beam-column elements with seven elements above the pile cap. The fiber section is discretized into mild longitudinal reinforcement, cover concrete, and core concrete fibers. In particular, the axial stress-strain behavior of concrete fibers is represented by uniaxial material *Concrete02* corresponding to the Kent-Scott-Park model [31] in compression and linear softening behavior in tension, as presented in Fig. 15c. The tension strength f_t and linear tension softening stiffness are 10% of the cylinder

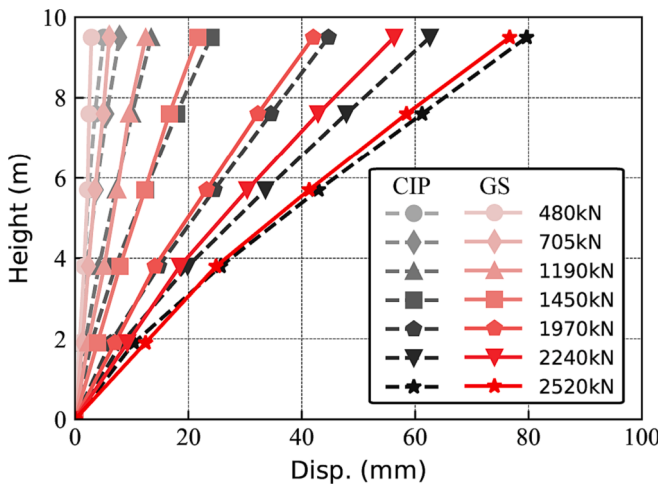


Fig. 11. Comparison of column deformation with various lateral loads.

compressive strength f_c and 10% of initial stiffness E_0 , respectively. The longitudinal steel reinforcements are simulated using uniaxial material *ReinforcingSteel*. The elastic modulus is 200 GPa, and tangent at initial strain hardening is taken as 3% of elastic modulus [6]. *Steel02* material considering post-tensioned stress is used to represent the mechanical behavior of unbonded PT strands. The modulus of elasticity E_s , yield strength f_s , and hardening ration γ_s are set as 195 GPa, 1860 MPa, and 0.001 [28]. Strand nodes move following the column nodes except for the vertical direction, which is achieved by the equal degree-of-freedom (Equal DOF) technique. Based on previous investigations [17,32], the average stress-strain behavior of GSSCs can be simulated by steel bars with amplified diameters. Thus in sections with grouted sleeves (e.g., within the range of 0.81 m above the pile cap top surface), the diameter of strengthened bars is set as 64 mm, so the area is identical to the sum of the grouted sleeve and 40-mm-diameter longitudinal bar.

A fiber-based *zero-length section* element is introduced at the base of the tested columns to capture the strain penetration effects of longitudinal reinforcements. It is worth noting that the *zero-length section* element is based on the plane hypothesis, which is not precisely abided by the joint section at the column-to-foundation interface [33]. But previous investigations have indicated that the macroscopic response of joint sections can be estimated appropriately based on plane section assumption [19,34,35]. The uniaxial material *Bond_SP01*, developed by Zhao and Sridharan [36], is used to represent the stress-slip relationship. It is worth noting that provided empirical formulas of yield slip s_y and ultimate slip s_u are acquired in accordance with experimental data with a bar diameter of less than 30 mm. Murcia-Delso et al. [37] proposed updated equations for large-diameter bars and validated them with

experimental results:

$$s_y = \frac{f_y^2 d_b}{12 E_b \tau_e} \quad (1)$$

$$s_u = \frac{f_y^2 d_b}{12 E_b \tau_e} + \frac{(\varepsilon_u + \varepsilon_y)(f_u - f_y)d_b}{8 \tau_p} \quad (2)$$

where d_b is the bar diameter, f_y and f_u are the yield and ultimate strength of bars, E_b is the elastic modulus of bars, τ_e and τ_p are average elastic bond stress and post-yield bond stress, which are set as $0.31 f_c^{0.75}$ and $0.23 f_c^{0.75}$, respectively. Moreover, *Bond_SP01* material is in series with *ReinforcingSteel* material to account for the debonding of dowel bars. The stress-displacement relationship of the debonding bars is calculated from the bar stress-strain relationship by multiplying strains by the debonding length (5 cm). The anchorage length of bars is much longer than the requirement (approximately 1.59 m) for the adopted equations [37]. The stress-displacement relationship of compressive concrete fiber is calculated by multiplying an assumed effective depth d_{comp} by the concrete strain [38]. The residual strength is modified to 80% of the concrete peak strength since the joint section concrete in the pile cap is well confined, and concrete crushing is not observed in the test [36]. The assumed effective depth is illustrated in Fig. 15g. The assumed depth value is optimized by comparison with the test result and is set as 2 m (the section width of tested columns).

The comparison of backbone curves between the experimental and numerical results is illustrated in Fig. 10. It is observed that numerical backbone curves match well with the experimental ones. The numerical

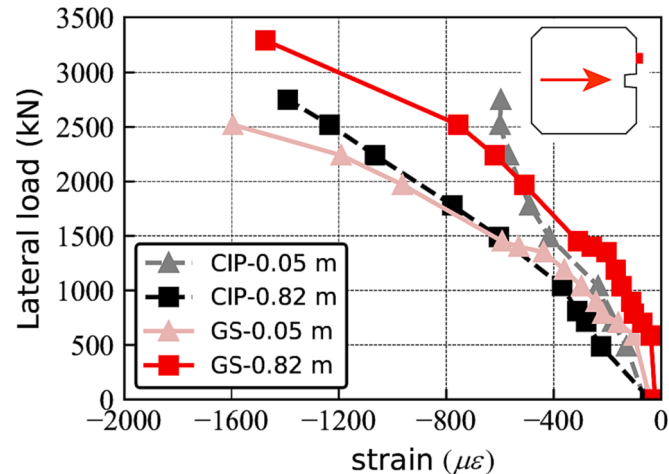


Fig. 13. Concrete strain at various heights to column base.

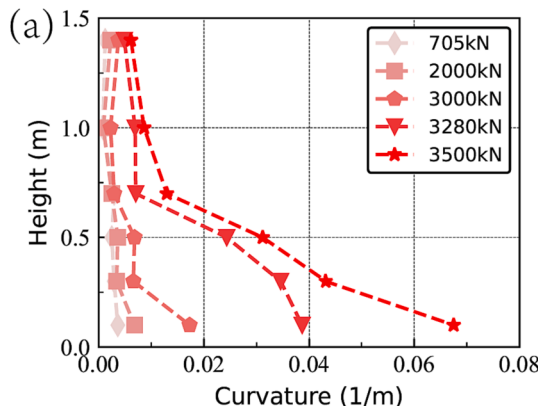


Fig. 12. Comparison of curvature with various lateral loads: (a) CIP column; (b) GS column.

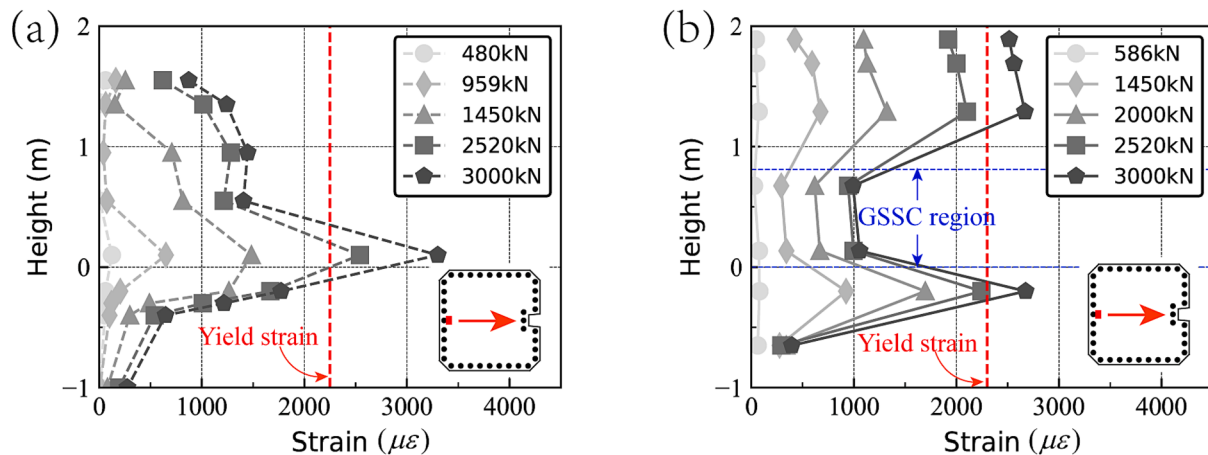


Fig. 14. Longitudinal reinforcement strain with various lateral loads: (a) CIP column; (b) GS column.

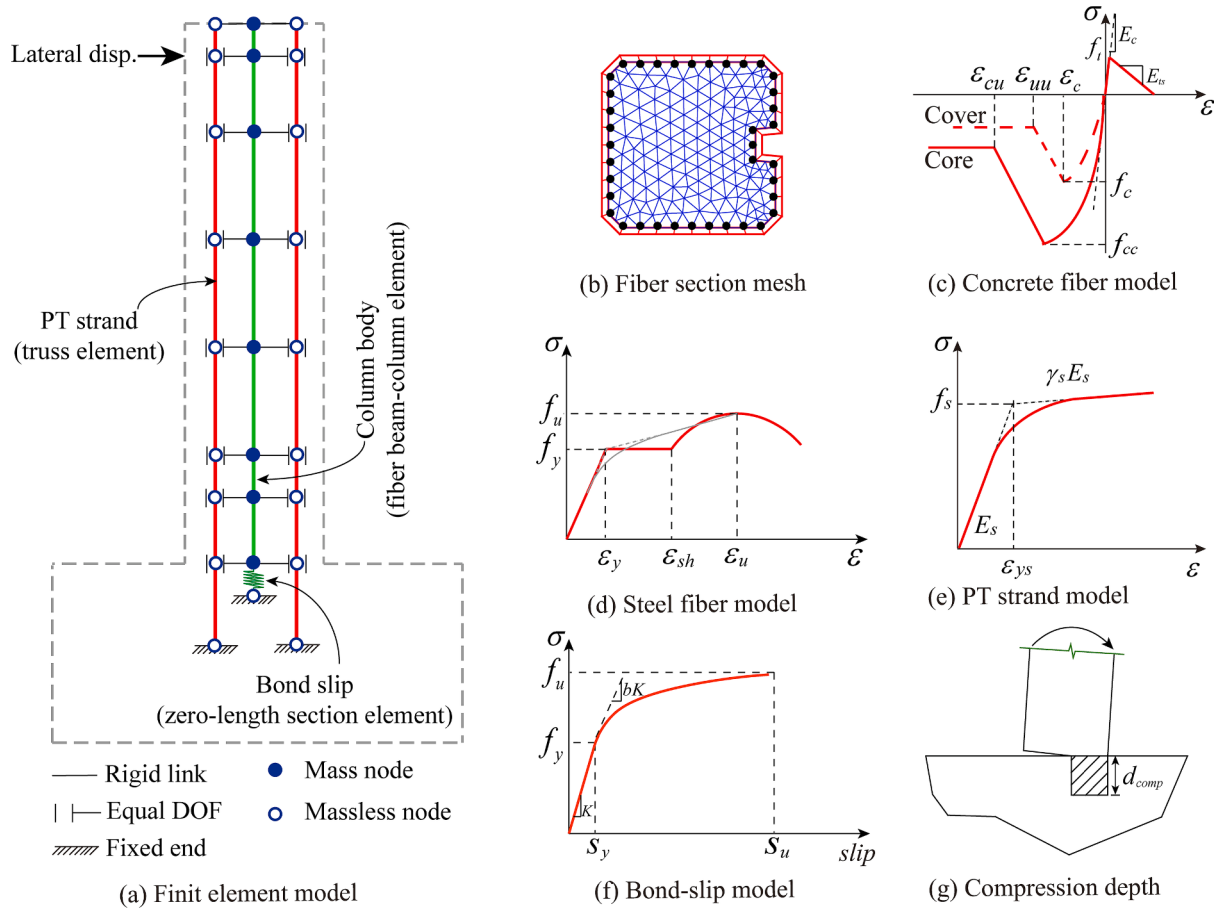


Fig. 15. Schematic illustration of the finite element model.

maximum lateral load of the CIP column is 2.9 % larger than the experimental one, which can be attributed to the construction errors in strand arrangement. The numerical curve of the GS pier fails to catch the capacity degrading because unexpected stirrup failure is not considered in the FE model. It is worth noticing that stirrup failure occurs after the GS column reaches its maximum lateral loading capacity, which means the lateral loading capacity is still dominated by the joint section. To eliminate the influence of variant axial force induced by unbonded PT strands, unbonded PT strands are substituted by a constant axial force of 12,875 kN. The backbone curve of the model without strands is also

illustrated in Fig. 10. Compared to the model with strands, the maximum lateral load capacity declines by 9.9% and 8.8% for the CIP column and GS column, respectively.

Fig. 16 presents and compares the joint opening in the GS column and the CIP one. The joint opening of two tested columns is approximately identical before the first yield of longitudinal bars. After that, a significantly larger joint opening is observed in GS columns. This phenomenon could be explained by the strain concentration in the column-to-foundation interface and the debonding of longitudinal bars below grouted sleeves. The numerical results of the GS pier match well with the

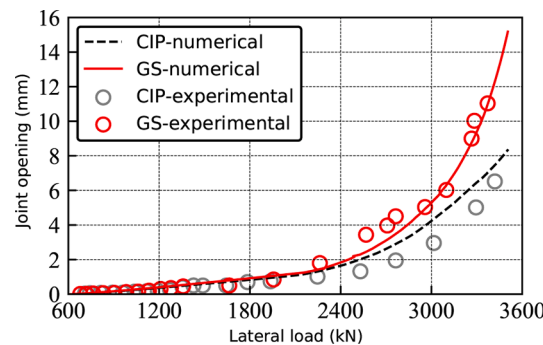


Fig. 16. Comparison of joint opening.

experimental ones indicating that the numerical model could effectively represent the effect of strain penetration. However, the FE model overrates the joint opening of the CIP column, which can mainly be attributed to the full development of multiple cracks in the plastic hinge region.

5. Simplified simulation method for strain penetration effects

As the above results indicated, the fiber-based analysis method can accurately account for strain penetration effects, but the modeling complexity limits its application seriously. So a simplified method to consider strain penetration effects need to be developed. As illustrated in Fig. 17, the rotation at the column end due to the slip of reinforcing bars θ_{slip} is defined by the bar deformation to the distance from the reinforcement to the neutral axis c_t . If the anchorage length of longitudinal bars is greater than the required development length $l_e + l_p$, yield slip s_y and ultimate slip s_u for a bar are given by Eq (1)-(2). Realizing that ε_b/c_t equals the curvature of the column-to-foundation section ϕ_y , the rotation for the first yield of longitudinal bars can be written as:

$$\theta_{yj} = \left(\frac{f_y d_b}{12\tau_e} + l_d \right) \phi_y = \left(\frac{f_y d_b}{12\tau_e} + l_d \right) \frac{M_y}{E_c I_{eff}} \quad (3)$$

where l_d is the debonded length of the longitudinal bars ($l_d=0$ cm and 5 cm for the tested CIP and GS columns), EI_{eff} is the effective stiffness of the reinforced concrete column that can be evaluated by [39]:

$$l_e = \frac{f_y d_b}{4\tau_e} \quad l_p = \frac{(f_u - f_y) d_b}{4\tau_p}$$

$$\tau_e = 0.31 f_c^{0.75} \quad \tau_p = 0.23 f_c^{0.75}$$

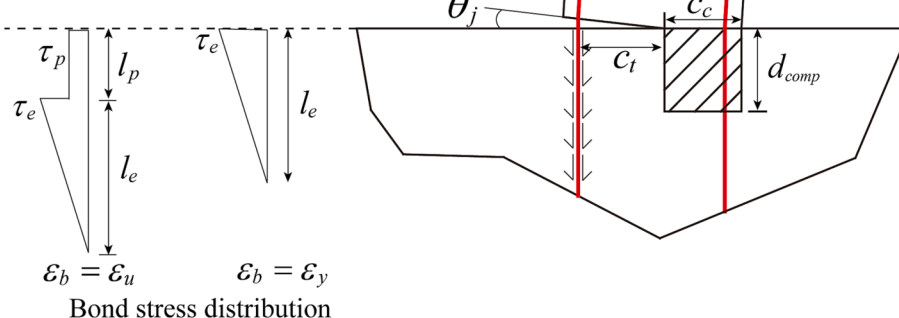


Fig. 17. Slip of longitudinal reinforcements from the foundation.

$$\frac{E_c I_{eff}}{E_c I_g} = \begin{cases} 0.2 & \text{if } P/A_g f_c \leq 0.2 \\ \frac{5}{3} \frac{P}{A_g f_c} - \frac{4}{30} & \text{if } 0.2 < P/A_g f_c \leq 0.5 \\ 0.7 & \text{if } 0.5 < P/A_g f_c \end{cases} \quad (4)$$

where A_g is the gross area of the column section, P is the axial force, E_c is the Young's modulus of concrete, I_g inertia moment of the column section. Although Eq (4) is proposed for CIP columns, it is also effective for GS columns in accordance with identical joint opening behavior before the first yield of longitudinal bars shown in Fig. 16. Then, the effective rotational stiffness of the column ends before the first yield of longitudinal bars can be expressed as:

$$K_{eff} = \frac{12\tau_e E_c I_{eff}}{f_y d_b + 12\tau_e l_d} \quad (5)$$

Berry and Eberhard [40] found an equation to approximate the plastic neutral axis depth for both round and rectangular columns:

$$\frac{D}{c_c} = 5.3 \left(1 + 9.4 \frac{P}{A_g f_c} \right)^{-1} \quad (6)$$

where D is the diameter or width of the column section. So the ultimate rotation can be given by:

$$\theta_{uj} = \frac{s_u + \varepsilon_u l_d}{D - c_c - c_0 - d_b/2} \quad (7)$$

where c_0 is the thickness of cover concrete, ε_u is bar ultimate strain, and the ultimate state corresponds to longitudinal bar fracture at the column-to-foundation interface or core concrete crushing of the column. It is worth noting that Eq (6) is proposed for CIP column sections and may not suit joint sections.

The maximum moment at the column-to-foundation section can be determined based on the plane hypothesis. Once the yield slip s_y , ultimate slip s_u and neutral axis depth c_c are obtained, the stress distribution of the joint section can be determined as illustrated in Fig. 18. The maximum bar deformation is $s_u + \varepsilon_u l_d$, while yield deformation is $s_y + \varepsilon_y l_d$. Considering the negligible concrete strength degradation, a uniform distribution of concrete stress is approximately simplified in the compression zone. So the ultimate moment of the joint section can be obtained by Eq (8) while precise bar stress is adopted.

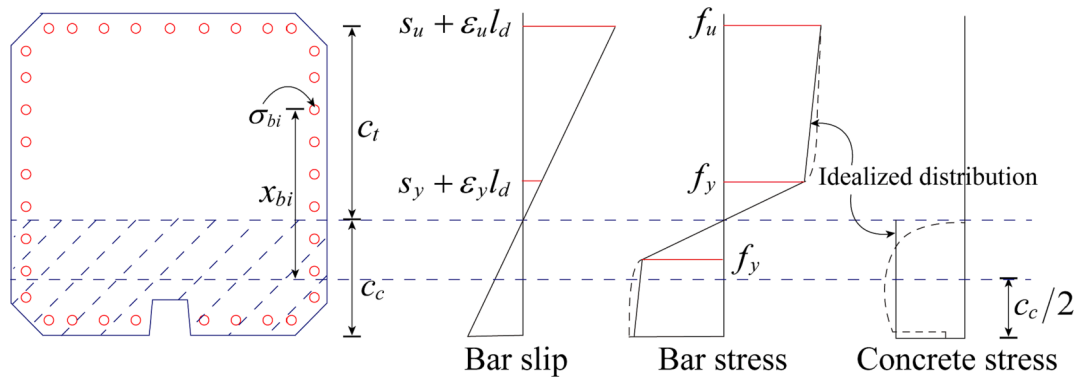


Fig. 18. Stress distribution under the plane hypothesis.

$$M_{uj} = \sum_{i=1}^N \sigma_{bi} A_{bi} x_{bi} + \frac{1}{2} P(D - c_c) \quad (8)$$

where N is the number of longitudinal bars, x_{bi} is the distance from i -th bar to the $1/2$ neutral axis depth, σ_{bi} and A_{bi} are stress and area of the i -th bar. To simplify the bar stress calculation, the distribution of bar stress is idealized to a bilinear curve, and a factor of 1.06 is used to consider the underrate of bar stress during idealization. The ultimate moment of the joint section can be rewritten as Eq (9) using idealized bar stress distribution.

$$M'_{uj} = 1.06 \sum_{i=1}^N \sigma'_{bi} A_{bi} x_{bi} + \frac{1}{2} P(D - c_c) \quad (9)$$

For CIP columns, M_{uj} is usually greater than the maximum moment of the column section M_{uc} because core concrete crushing of the column section may occur earlier than bar fracture. So the maximum lateral load capacity of the CIP column is M_{uc}/L . Regarding GS columns, the maximum lateral load capacity is determined by Eq (10).

$$F_{\max} = \min \left\{ \frac{M_{uj}}{L}, \frac{M_{uc}}{L - L_{gs}} \right\} \quad (10)$$

where L is the distance from the lateral loading point to the column-to-foundation interface, L_{gs} is the length of grouted sleeves.

To establish a plastic neutral axis depth estimation formula for the joint section, moment-rotation analyses are conducted for column-to-foundation sections with various design parameters and material-related uncertainty parameters. More specifically, the design parameters include: section width of the longer side (D), depth-to-width ratio of the section (γ_a), axial compression ratio ($\xi = P/A_g f_c$), longitudinal reinforcement ratio (ρ_L), and stirrup reinforcement ratio (ρ_T). Based on practical engineering applications, the lower and upper bounds of the design parameters are determined. The construction materials for joint sections are C40 concrete and HRB400 steel bars. The probability distribution, mean value, coefficient of variation (CV), or standard deviation (SD) of considered uncertainty parameters are listed in Table 4. The correlation coefficients of different pairs of uncertain parameters are assumed as follows: $\rho = 0.8$ for (1) ϵ_c and ϵ_{uu} , (2) f_{yl} and ϵ_{ul} , (3) f_{yl} and f_{ul} , (4) ϵ_{ut} and f_{yt} , $\rho = 0.65$ for ϵ_{ul} and f_{ul} , $\rho = 0$ for all other pairs of parameters [41]. Latin hypercube sampling (LHS) and Nataf transformation [42] techniques are adopted to establish one hundred studying cases.

Moment-rotation analyses for one hundred cases are conducted with an auto moment-curvature analysis program coded by the author (<https://github.com/Penghui0616/MCAAnalysis>). The stress-strain relationship of steel bars and concrete are replaced with the stress-displacement relationship mentioned in section 4. The plastic neutral axis depth of each studying case is acquired. And linear regression models are developed for both CIP and GS columns, as shown in Fig. 19. Compared to CIP columns, a debond length of 5 cm is considered for GS

Table 4
Considered parameters and their probability distribution.

Name	Description	Units	Distribution	Distribution parameters
<i>Design parameters</i>				
D	Section width of the longer side	m	Uniform	Lower = 1.0, Upper = 3.0
γ_a	Depth-to-width ratio		Uniform	Lower = 0.5, Upper = 1.0
ξ	Axial compression ratio		Uniform	Lower = 0.05, Upper = 0.3
ρ_L	Longitudinal reinforcement ratio	%	Uniform	Lower = 0.6, Upper = 2.5
ρ_T	Stirrup reinforcement ratio	%	Uniform	Lower = 0.4, Upper = 0.9
<i>Uncertainty parameters</i>				
f_c	Cover concrete compressive strength [28]	MPa	Normal	Mean = 40, SD = 4.8
ϵ_c	Cover concrete strain at peak strength [43]		Lognormal	Mean = 0.002, CV = 0.2
ϵ_{uu}	Cover concrete strain at crushing strength [43]		Lognormal	Mean = 0.006, CV = 0.2
f_{yl}	Yield strength of longitudinal bars [44]	MPa	Normal	Mean = 461, SD = 35.84
E_l	Young's modulus of steel rebar [43]	GPa	Lognormal	Mean = 201, CV = 0.033
f_{ul}	Ultimate strength of longitudinal bars [44]	MPa	Normal	Mean = 622, SD = 49.76
ϵ_{ul}	Ultimate strain of longitudinal bars [41]		Normal	Mean = 0.12, SD = 0.024
f_{yt}	Yield strength of stirrups [44]	MPa	Normal	Mean = 461, SD = 35.84
ϵ_{ut}	Ultimate strain of stirrups [41]		Normal	Mean = 0.12, SD = 0.024

column longitudinal bars at the joint section. Negligible differences are observed in the two regression models. So the neutral axis depth prediction equation is fitted considering both CIP and GS data sets:

$$\frac{c_c}{D} = 0.65 \frac{P}{A_g f_c} + 0.15 \quad (11)$$

The Moment-rotation relationship of a joint section can be idealized as a bilinear curve (shown in Fig. 20) following several criteria: (1) the elastic portion passes the point of initial yielding; (2) the post-yield portion passes the point of bar fracture; (3) the area under the original moment-rotation curve equals to that under the idealized curve. The simplified rotational spring is determined by four parameters: effective rotational stiffness K_{eff} , post-yield stiffness ratio γ_j , ultimate moment M_{uj} , and ultimate rotation θ_{uj} of the joint section. An empirical predicting equation for the post-yield stiffness ratio of the simplified bilinear constitutive is founded and fitted with the CIP and GS data sets, as illustrated in Fig. 21.

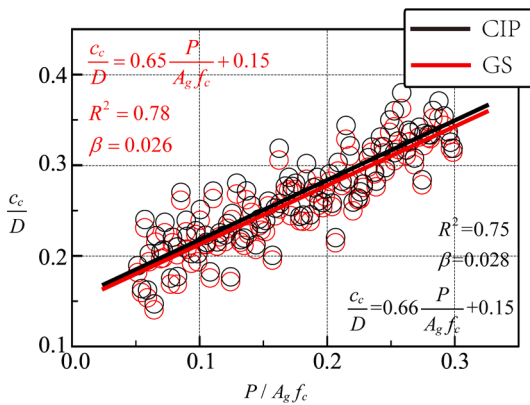


Fig. 19. Regression model for neutral axis depth of joint sections.

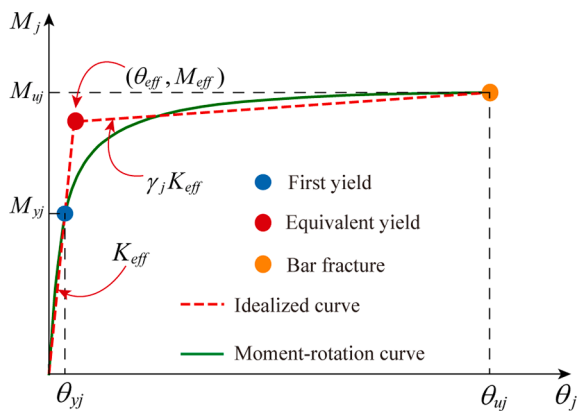


Fig. 20. Simplified bilinear constitutive relationship for strain penetration modeling.

$$\gamma_j = 0.2 \frac{M_{uj}/K_{eff}}{\theta_{uj} - M_{uj}/K_{eff}} - 0.006 \quad (12)$$

Then, the effective yield rotation θ_{eff} and effective yield moment M_{eff} can be expressed as:

$$\theta_{eff} = \frac{M_{uj} - \gamma_j K_{eff} \theta_{uj}}{(1 - \gamma_j) K_{eff}} \quad (13)$$

$$M_{eff} = \frac{M_{uj} - \gamma_j K_{eff} \theta_{uj}}{1 - \gamma_j} \quad (14)$$

Using Eq (5)-(12), the predicted model parameters are compared

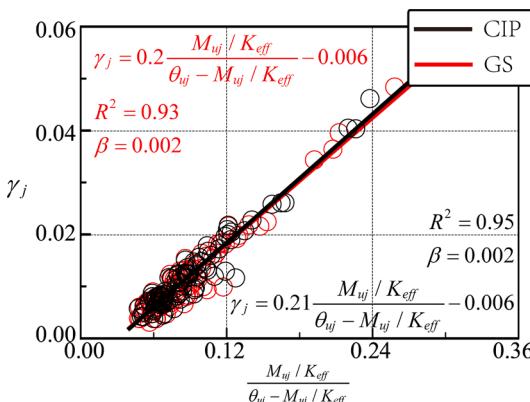


Fig. 21. Regression model for post-yield stiffness ratio.

with the calibrated parameters from the numerical analysis results. The ratio of predicted value to calibrated value is computed for each studying case, and statistical results are illustrated in Fig. 22. As can be observed, median values are 1.05, 0.98, 1.00, 0.99, and 0.99 for K_{eff} , M_{uj} , M_{uy} , θ_{uj} , and γ_j concerning CIP columns, and the corresponding values are 1.00, 0.98, 1.01, 0.99, and 0.96 for GS columns. The median values are close to 1.00, confirming the accuracy of the proposed prediction equation. Besides, M_{uj} and M_{uy} are predicted with the lowest standard deviation followed by θ_{uj} , indicating the availability of ultimate moment estimation based on idealized bar stress distribution.

The numerical simulation results of full-scale tests with constant axial load are conducted herein to validate the proposed simulation method for strain penetration effects. Moment-rotation curves and the simplified bilinear constitutive based on calibrated and prediction parameters are obtained, as illustrated in Fig. 23a and c. As observed, the predicted bilinear curves are generally close to the calibrated ones, confirming the effectiveness of Eq (5)-(14). Steel01 material in OpenSeesPy is used to simulate the simplified moment-rotation relationship of joint sections with predicted parameters. Consequently, a zero-length element with simplified bilinear constitutive is set at the column-to-foundation interface, while the fiber-based zero-length section element is eliminated. Fig. 23b compares the backbone curves of the CIP column with the fiber-based strain penetration model, simplified bilinear model, and none strain penetration model. The backbone curve with a simplified strain penetration model has similar initial stiffness and ultimate rotation to the backbone curve with a fiber-based model. In contrast, the backbone curve considering none strain penetration effects overestimates the initial stiffness and underestimates the ultimate displacement. Because the lateral loading capacity of the CIP column is dominated by the column body, all backbones have the same yield and ultimate strength. Fig. 23d makes a comparison of GS column backbones in various conditions. It is clear that the simplified modeling results can well match the results of the fiber-based strain penetration model. The FE model without strain penetration presents failure induced by core concrete crushing of the column body. So higher ultimate strength and lower lateral displacement capacity are observed.

6. Conclusions

A full-scale precast bridge column with grouted sleeve (GS) connections and large-diameter (40 mm) reinforcing bars has been experimentally investigated with comparison to a reference cast-in-place (CIP) column in this study. The specimen design is based on the actual segmental expressway bridge in Shaoxing. Therefore, this study investigated and verified the mechanical performance of GS columns (i.e., lateral loading capacity, displacement capacity, and ductility). Finite element models were established at the OpenSeesPy platform and validated against experimental results. A simplified bilinear rotational spring was proposed to simulate strain penetration in GS and CIP columns. The availability of the simplified simulation method of strain penetration effects was confirmed with the numerical simulation results of full-scale tests. Conclusions are drawn as follows:

- According to the tensile tests of grouted splice sleeve couplers (GSSCs), an embedded length of $10D_s$ (where D_s is the diameter of connected bars of 40 mm) was selected to avoid bar pull-out failure and sleeve fracture. No damage in GSSCs was observed during the full-scale static test indicating the sufficiency of embedded length.
- The CIP column exhibited a typical flexural failure with the longitudinal bar fracture, while the GS column presented a failure by bar buckling and concrete crush induced by stirrup straightening without longitudinal bar fracture. It is suggested that stirrups with 90-degree hooks should be welded into closed stirrups at the region of the GSSC. In addition, more stirrups are conservatively suggested to arrange in the area.

Median:	1.05	0.98	1.00	0.99	0.99	1.00	0.98	1.01	0.99	0.96
SD:	0.68	0.02	0.02	0.04	0.22	0.60	0.02	0.02	0.03	0.24

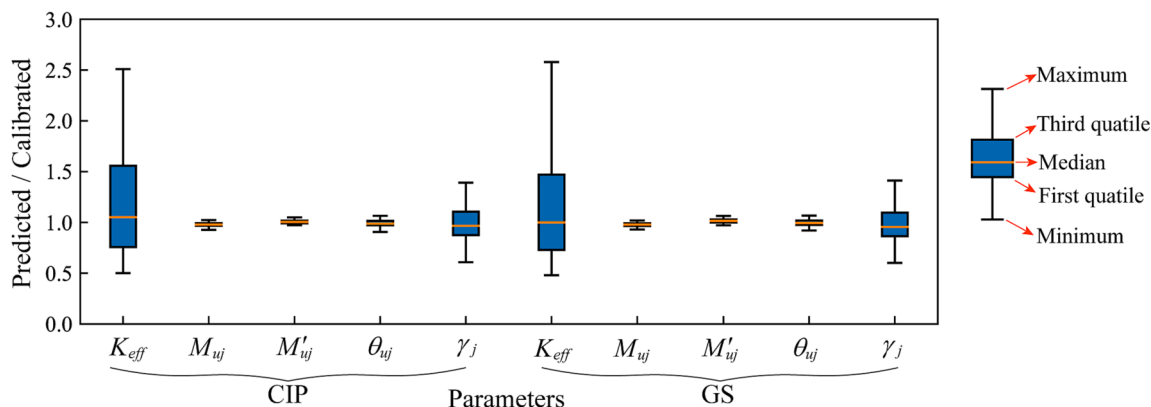


Fig. 22. Statistical comparison among the ratios of predicted to calibrated values of model parameters.

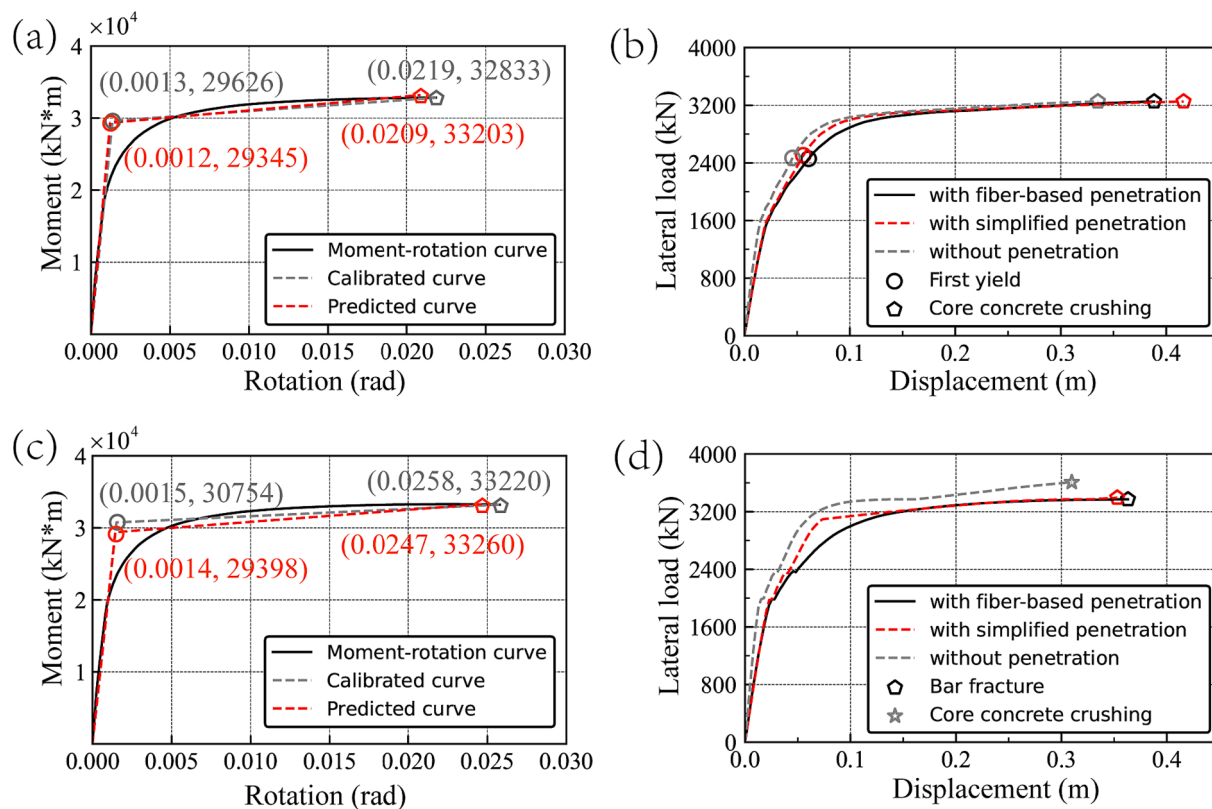


Fig. 23. Model validation: (a) moment-rotation analysis of CIP joint section; (b) backbone curves of the CIP column; (c) moment-rotation analysis of GS joint section; (d) backbone curves of the GS column.

- The crack pattern, deformations, and resistance mechanism of the GS column are different from the CIP column. The first yield and maximum lateral load of the GS column are 6%, 5% larger than the CIP column, and the ultimate lateral displacement of the GS column is 96% of the CIP column due to differences in failure modes.
- The numerical models matched well with the backbone curves and joint opening of the test GS column. However, the FE model overrates the joint opening of the CIP column, which can mainly be attributed to the full development of multiple cracks in the plastic hinge region.
- The proposed empirical equation can precisely predict effective rotational stiffness, post-yield stiffness ratio, ultimate moment, and

ultimate rotation of joint sections. A simplified bilinear rotational spring with predicted parameters is effective in simulating strain penetration in GS and CIP columns.

CRediT authorship contribution statement

Penghui Zhang: Methodology, Data curation, Investigation, Writing – original draft. **Zhiqiang Wang:** Conceptualization, Supervision, Funding acquisition, Writing – review & editing. **Jiping Ge:** Conceptualization, Supervision, Funding acquisition, Data curation, Writing – review & editing. **Xingfei Yan:** Resources, Investigation. **Side Liu:**

Resources, Investigation.

Declaration of Competing Interest

The authors declare that they have no known competing financial interests or personal relationships that could have appeared to influence the work reported in this paper.

Data availability

Data will be made available on request.

Acknowledgment

This research was supported by the National Natural Science Foundation of China under Grant No. 51978511, 51778470; China Railway 22nd Bureau Group 3rd Engineering Corporation Limited under Grant No. CR2203-S2-SX308-JS-2021-009; Shanghai Science and Technology Commission under Grant No. 2100240100.

References

- [1] Qu H, Li T, Wang Z, Wei H, Shen J, Wang H. Investigation and verification on seismic behavior of precast concrete frame piers used in real bridge structures: Experimental and numerical study. *Eng Struct* 2018;154:1–9.
- [2] Liu Y, Li X, Zheng X, Song Z. Experimental study on seismic response of precast bridge piers with double-grouted sleeve connections. *Eng Struct* 2020;221:111023.
- [3] Ameli MJ, Brown DN, Parks JE, Pantelides CP. Seismic column-to-footing connections using grouted splice sleeves. *ACI Struct J* 2016;113:1021–30.
- [4] Liu H, Chen J, Xu C, Du X. Seismic performance of precast column connected with grouted sleeve connectors. *J Build Eng* 2020;31:101410.
- [5] Qu H, Fu J, Li T, Wu C, Sun X, Wei H, et al. Experimental and numerical assessment of precast bridge columns with different grouted splice sleeve coupler designs based on shake table test. *J Bridg Eng* 2021;26(8):04021055.
- [6] Wang Z, Qu H, Li T, Wei H, Wang H, Duan H, et al. Quasi-static cyclic tests of precast bridge columns with different connection details for high seismic zones. *Eng Struct* 2018;158:13–27.
- [7] Haber ZB, Mackie KR, Al-Jelawy HM. Testing and analysis of precast columns with grouted sleeve connections and shifted plastic hinging. *J Bridg Eng* 2017;22:04017078.
- [8] Liu Z, Lei H, Tong T, Wu S, Lu G. Precast segmental piers: testing, modeling and seismic assessment of an emulative connection based on a grouted central tenon. *Bull Earthquake Eng* 2022;20(5):2529–64.
- [9] Wang Z, Zhang P, Zhang J, Li T, Yan X, Qu H. Seismic performance comparison of precast bridge columns with different shear span-to-depth ratios and connection designs via quasi-static cyclic test. *J Bridg Eng* 2022;27:4022094.
- [10] Wang J, Shen Y, Li G, Chen M, Fan C. Quasi-full-scale experimental study on bridge precast concrete columns under static loading. *J Bridg Eng* 2021;26:1–15.
- [11] Steck KP, Eberhard MO, Stanton JF. Anchorage of large-diameter reinforcing bars in ducts. *ACI Struct J* 2009;106:506.
- [12] Raynor DJ, Lehman DE, Stanton JF. Bond-slip response of reinforcing bars grouted in ducts. *Struct J* 2002;99:568–76.
- [13] Liang X, Wang J, Wang Y, Xiang H, Feng Q, Xu R. Analytical model of grouted sleeve connector and its solution based on the state space method. *Constr Build Mater* 2022;341:127708.
- [14] Yang C, Zhang L, Zhang Z, Cao X, Khan I, Deng K, et al. Effective stress-strain relationship for grouted sleeve connection: Modeling and experimental verification. *Eng Struct* 2020;210:110300.
- [15] Al-Jelawy HM. Experimental and numerical investigations on monotonic tensile behavior of grouted sleeve couplers with different splicing configurations. *Eng Struct* 2022;265:114434.
- [16] Haber ZB, Saiidi MS, Sanders DH. Behavior and simplified modeling of mechanical reinforcing bar splices. *ACI Struct J* 2015;112:179–88.
- [17] Tazav M, Saiidi MS. Seismic design of bridge columns incorporating mechanical bar splices in plastic hinge regions. *Eng Struct* 2016;124:507–20.
- [18] Culmo MP, Marsh L, Stanton J, Mertz D. Recommended AASHTO guide specifications for ABC design and construction. 2018.
- [19] Wang R, Ma B, Chen X. Seismic performance of pre-fabricated segmental bridge piers with grouted splice sleeve connections. *Eng Struct* 2021;229:111668.
- [20] Ding M, Xu W, Wang J, Chen Y, Du X, Fang R. Seismic performance of prefabricated concrete columns with grouted sleeve connections, and a deformation-capacity estimation method. *J Build Eng* 2022;55:104722.
- [21] DB J52/T105-2021 Technical specification for detection of filling plumpness of sleeve grouting in fabricated concrete structures. China: Housing and Urban-Rural Construction. Management Committee of Guizhou; 2021.
- [22] GBT 50081-2002 Standard for test method of mechanical properties of normal concrete. Beijing: Ministry of Housing and Urban-Rural Development of China; 2012.
- [23] GBT 17671-1999 Method of testing cements: Determination of strength. Beijing: State Bureau of Quality and Technical Supervision; 1999.
- [24] GB 50010-2010 Code for design of concrete structures. Beijing: Ministry of Housing and Urban-Rural Development of the People's Republic of China; 2015.
- [25] Lin F, Wu X. Mechanical performance and stress-strain relationships for grouted splices under tensile and cyclic loadings. *Int J Concr Struct Mater* 2016;10(4):435–50.
- [26] Ma G, Qin C, Hwang H-J, Zhou Z. Data-driven models for predicting tensile load capacity and failure mode of grouted splice sleeve connection. *Eng Struct* 2023;289:116236.
- [27] DG/TJ 08-2160-2021 Technical specification for prefabricated Bridge. China: Housing and Urban-Rural Construction Management Committee of Shanghai; 2021.
- [28] JTG 3362-2018 Specifications for design of highway reinforced concrete and prestressed concrete bridges and culverts. China: Ministry of Transportation, People's Republic of China; 2018.
- [29] Priestley MJN, Park R. Strength and ductility of concrete bridge columns under seismic loading. *Struct J* 1987;84:61–76.
- [30] Zhu M, McKenna F, Scott MH. OpenSeesPy: Python library for the OpenSees finite element framework. *SoftwareX* 2018;7:6–11.
- [31] Scott BD, Park R, Priestley MJN. Stress-strain behavior of concrete confined by overlapping hoops at low and high strain rates. *J Proc* 1982;79:13–27.
- [32] Xu W, Biao M, Huang H, Su J, Li J, Wang R. The seismic performance of precast bridge piers with grouted sleeves. *Eng Mech* 2020;37:93–104.
- [33] Tullini N, Minghini F. Cyclic test on a precast reinforced concrete column-to-foundation grouted duct connection. *Bull Earthq Eng* 2020;18(4):1657–91.
- [34] Wang X, Fang J, Zhou L, Ye A. Transverse seismic failure mechanism and ductility of reinforced concrete pylon for long span cable-stayed bridges: Model test and numerical analysis. *Eng Struct* 2019;189:206–21.
- [35] Blanco G, Ye A, Wang X, Goicoechea JM. Parametric pushover analysis on elevated RC pile-cap foundations for bridges in cohesionless soils. *J Bridg Eng* 2019;24:04018104.
- [36] Zhao J, Sritharan S. Modeling of strain penetration effects in fiber-based analysis of reinforced concrete structures. *ACI Mater J* 2007;104:133.
- [37] Murcia-Delso J, Jawawaz G. Analytical model for bar slip and pullout capacity of straight bars. *ACI Struct J* 2019;116:137–49.
- [38] Berry MP, Eberhard MO. Performance modeling strategies for modern reinforced concrete bridge. California: Pacific Earthquake Engineering Research Center; 2007.
- [39] Elwood KJ, Eberhard MO. Effective stiffness of reinforced concrete columns. *ACI Struct J* 2009;106.
- [40] Berry MP, Eberhard MO. Performance models for flexural damage in reinforced concrete columns. California: Pacific Earthquake Engineering Research Center; 2003.
- [41] Zhou L. Probability-based performance and post-earthquake functionality assessment for pile supported bridges under combined effects of scour and earthquake hazards. Shanghai: Tongji University; 2022.
- [42] Liu P-L, Der Kiureghian A. Multivariate distribution models with prescribed marginals and covariances. *Probabilistic Eng Mech* 1986;1(2):105–12.
- [43] Barbato M, Gu Q, Conte JP. Probabilistic push-over analysis of structural and soil-structure systems. *J Struct Eng* 2010;136(11):1330–41.
- [44] GB/T 1499.2-2018 Steel for the reinforcement of concrete Part 2: Hot rolled ribbed bars. Standardization Administration of People's Republic of China; 2018.